



HAL
open science

Nonlinear Terahertz electroluminescence from Dirac-Landau polaritons

B. Benhamou-Bui, C. Consejo, S. Krishtopenko, S. Ruffenach, C. Bray, J. Torres, J. Dzian, F. Le Mardelé, A. Pagot, X. Baudry, et al.

► To cite this version:

B. Benhamou-Bui, C. Consejo, S. Krishtopenko, S. Ruffenach, C. Bray, et al.. Nonlinear Terahertz electroluminescence from Dirac-Landau polaritons. 2025. <hal-05408435>

HAL Id: hal-05408435

<https://cnrs.hal.science/hal-05408435v1>

Preprint submitted on 10 Dec 2025

HAL is a multi-disciplinary open access archive for the deposit and dissemination of scientific research documents, whether they are published or not. The documents may come from teaching and research institutions in France or abroad, or from public or private research centers.

L'archive ouverte pluridisciplinaire HAL, est destinée au dépôt et à la diffusion de documents scientifiques de niveau recherche, publiés ou non, émanant des établissements d'enseignement et de recherche français ou étrangers, des laboratoires publics ou privés.



HAL Authorization

Nonlinear Terahertz electroluminescence from Dirac–Landau polaritons

B. Benhamou-Bui¹, C. Consejo¹, S.S. Krishtopenko¹, S. Ruffenach¹, C. Bray¹, J. Torres¹, J. Dzian², F. Le Mardele², A. Pagot³, X. Baudry³, S.V. Morozov^{4,5}, N.N. Mikhailov^{6,7}, S.A. Dvoretzki^{7,8}, B. Jouault¹, P. Ballet³, M. Orlita², C. Ciuti⁹, F. Teppe¹

¹ *Laboratoire Charles Coulomb (L2C), UMR 5221 CNRS – Université de Montpellier, F-34095 Montpellier, France*
² *Laboratoire National des Champs Magnétiques Intenses, CNRS – UGA – UPS – INSA – EMFL, Grenoble, France*
³ *CEA, LETI, MINATEC Campus, DOPT, Grenoble, France*
⁴ *Institute for Physics of Microstructures of the Russian Academy of Sciences, Nizhny Novgorod, Russia*
⁵ *Lobachevsky State University of Nizhny Novgorod, Nizhny Novgorod, Russia*
⁶ *A.V. Rzhanov Institute of Semiconductor Physics, Siberian Branch of the Russian Academy of Sciences, Novosibirsk, Russia*
⁷ *Novosibirsk State University, Novosibirsk, Russia*
⁸ *Tomsk State University, Tomsk, Russia and*
⁹ *Université Paris Cité, CNRS, Matériaux et Phénomènes Quantiques, 75013 Paris, France*

We report the observation of Dirac–Landau polaritons via THz magnetorefectivity spectroscopy, demonstrating strong coupling between cyclotron transitions of two-dimensional Dirac fermions in HgTe quantum wells and optical cavity modes. We demonstrate efficient nonlinear electroluminescence, characterized by a strongly out-of-equilibrium polariton distribution dominated by emission from the upper polariton branches. Model calculations, based on the nonlinear dependence of the emission intensity and spectral narrowing with bias voltage, indicate a polariton occupancy per mode close to unity, with a significant contribution from stimulated polariton emission. These findings open promising prospects for the development of Dirac–Landau polariton condensates and low-threshold, tunable terahertz polariton lasers based on cyclotron emission.

Introduction — Dirac materials [1], characterized by their relativistic-like electronic band structures, exhibit low carrier mass and a strongly non-equidistant Landau level spectrum in the presence of a magnetic field. These combined features suppress non-radiative Auger recombination arising from Coulomb electron-electron interactions and enable cyclotron emission [2–4] with remarkable tunability at low magnetic fields [5, 6], a functionality that was not achievable in p-Ge Landau level lasers where the larger effective mass of holes required the use of high magnetic fields [7–11]. In HgTe quantum wells near the topological phase transition [12, 13], the resulting Terahertz (THz) cyclotron emission has been experimentally demonstrated and shown to be tunable not only by magnetic field and carrier density, but also by gate voltage at a fixed magnetic field [14, 15]. These characteristics make Dirac systems appealing not only for their distinctive topological properties [16], but also for exploring non-equilibrium carrier dynamics in unconventional configurations and for advancing next-generation THz optoelectronic devices. Nonetheless, the physical realization of stimulated photon emission in Dirac materials remains challenging, as achieving electron population inversion typically requires electric fields approaching the breakdown limit of the system.

In parallel, the regime of strong light-matter coupling has enabled the emergence of hybrid bosonic quasiparticles known as polaritons, which exhibit unique quantum fluid behavior [17] and can undergo condensation and lasing without requiring electronic population inversion [18, 19]. Exciton-polariton lasers have been demon-

strated across a broad range of material systems [20–26], yet no polariton laser based on inter-Landau level transitions has been realized to date. Landau polaritons — resulting from the coupling between Landau level transitions and confined photonic modes — were theoretically predicted over a decade ago [27] and subsequently observed through reflectivity and transmission measurements in conventional semiconductor two-dimensional electron gases [28–30]. Recent experiments have expanded this concept, revealing novel features and strong coupling regimes in a variety of platforms [31–36]. The coexistence of Dirac Landau levels and the strong light-matter coupling regime opens the door to a novel physical platform with potentially unprecedented properties, holding exciting promise for THz polariton condensates and lasers.

In this Letter, we observe the formation of Dirac–Landau polaritons in HgTe quantum wells, resulting from the strong coupling between cyclotron transitions of two-dimensional Dirac fermions and THz cavity modes. Magneto-reflectivity measurements reveal clear anticrossings between cavity modes and Landau level transitions, confirming the hybrid light-matter nature of the excitations. We demonstrate electroluminescence from these polaritons under pulsed electrical excitation, with the emission spectrum measured in crossed electric and magnetic fields. The emission peaks coincide with the polariton branches extracted from reflectivity, and the nonlinear dependence on bias voltage, along with spectral narrowing, indicates a polariton occupancy per mode close to unity and an important contribution from

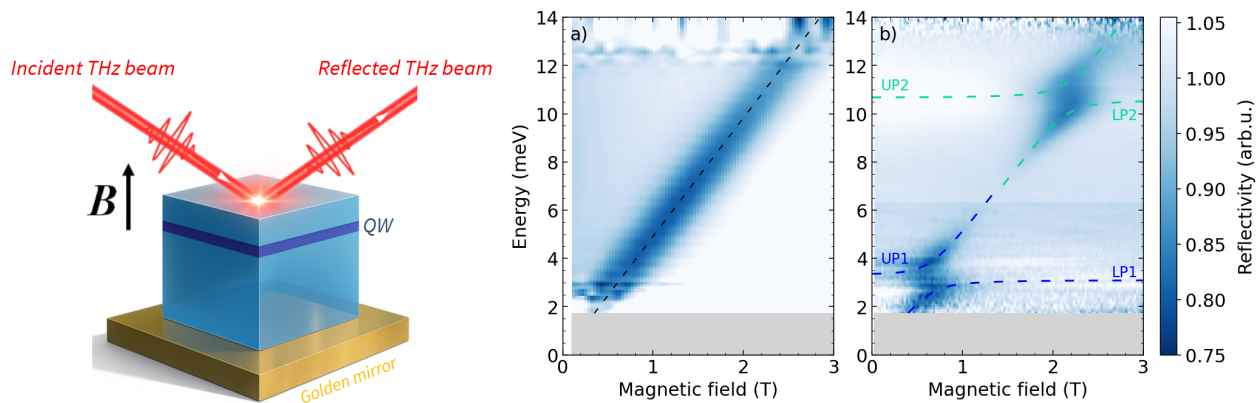


FIG. 1. Left panel: Sketch of the physical system, consisting of a 2D material hosting Dirac fermions embedded in a THz cavity resonator. A magnetic field B is applied perpendicular to the plane of the 2D material, inducing Landau quantization of the electronic states. The optical response of the system is probed via reflection spectroscopy using an incident THz beam. Right panel: Magneto-reflectivity spectra (a) without a cavity and (b) with a cavity resonator. In the absence of a cavity, the color plot shows a linear evolution of the cyclotron energy with increasing magnetic field. The 2D material in Sample A is an 8 nm-thick HgTe quantum well measured at $T = 4.2$ K. In the presence of a 28 μm -thick cavity, the cyclotron dispersion displays clear spectral anti-crossings at magnetic fields of 0.7 T and 2 T, corresponding to energies of approximately 3 meV and 10 meV, respectively.

stimulated polariton emission.

Dirac-Landau polaritons — The polariton excitations of a cavity-embedded two-dimensional electron gas in the presence of a magnetic field can be described by a bosonic quantum Hamiltonian[27] of the form $H = H_{cavity} + H_{Landau} + H_{int} + H_{dia}$, where H_{cavity} is the bare Hamiltonian of the cavity, H_{Landau} describes the collective cyclotron excitation of the electrons occupying the Landau levels, H_{int} is the paramagnetic light-matter interaction, while H_{dia} is the diamagnetic contribution [27]. Note that this effective Hamiltonian contains only bosonic operators corresponding to the photon cavity and to the cyclotron excitation mode. The matter component of a Landau polariton is a collective cyclotron excitation: this was first demonstrated for GaAs/AlGaAs quantum wells, where the band structure is parabolic [28]. However, collective cyclotron excitations can occur also with non-parabolic band structures, as previously observed in Ref. 32, or even in Dirac systems exhibiting linear band dispersion. Indeed, the cavity quantum electrodynamics of graphene [37–39] has been theoretically investigated in the ultrastrong coupling regime, where the existence of ground state instabilities is debated due to the role of the diamagnetic term in effective theories. In the ultrastrong coupling regime [40], achieved when the polariton coupling becomes comparable to the cavity and cyclotron transition frequencies, the diamagnetic interaction plays a major role. Instead, in this work, we will concentrate on excited states (polaritons) in the strong coupling regime, that is, in a regime with moderate diamagnetic corrections and we will focus on the remarkable nonlinear emission properties of electrically driven Dirac-Landau polaritons.

In order to study the cyclotron emission from these Dirac-Landau polaritons, it is necessary to first achieve the strong coupling regime between a resonant THz cavity and the cyclotron resonance of Dirac fermions. To achieve this, we performed THz magneto-absorption spectroscopy (see Fig. 1). The selected system consists of a HgTe-based quantum well close to the gapless state (with a low-energy band structure represented by Dirac fermions), placed within an optical cavity designed for THz cyclotron frequencies [see Fig. 1 and 2]. To create the THz Fabry-Perot cavity with enhanced photon confinement and hence light-matter interaction, the substrate (GaAs for sample A and B and CdTe for sample C) of the quantum well was thinned. Before measuring the samples via magneto-reflectivity, we employed two characterization methods. The first one involved measuring multiple substrates with thicknesses ranging from 300 μm to 40 μm via THz Time Domain Spectroscopy (TDS). The second method involved directly measuring the same samples in emitter mode by detecting the thermal radiation emitted at zero magnetic field, while the sample was electrically heated. Both approaches confirmed the existence of an optical cavity formed within the sample substrates, as shown in the Supplementary Material (SM). The narrowest cavity was then analyzed using relative magneto-reflectivity measurements to characterize the coupling between the cyclotron resonance and the cavity modes. These results are compared to identical measurements taken without THz cavity (see Fig. 1a and b).

The magneto-reflectivity results obtained without the cavity clearly reveal a cyclotron resonance whose energy evolves linearly with the applied magnetic field. The

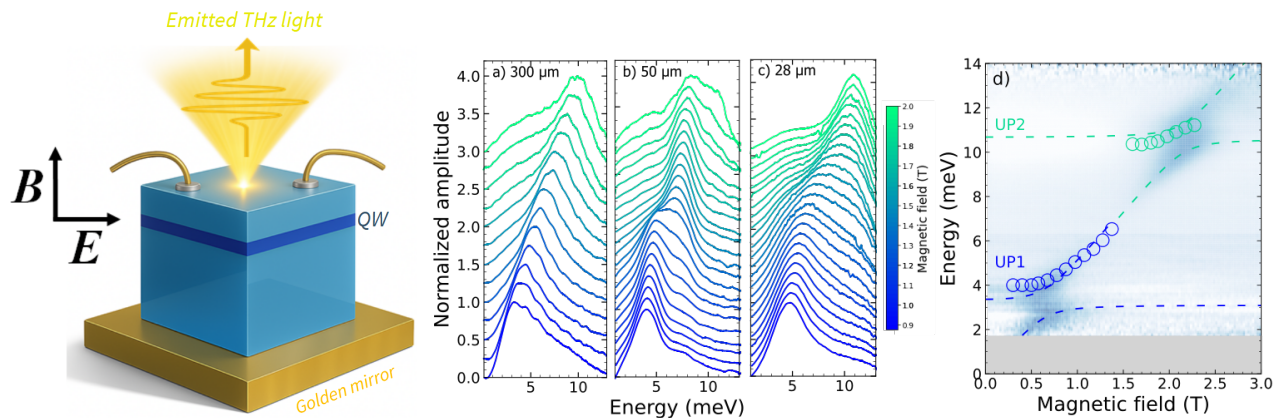


FIG. 2. Left panel: sketch of the THz electroluminescent cavity device, where an in-plane electrical bias injects current between source and drain ohmic contacts. Right panel: THz emission spectra at various magnetic fields, shown for different device configurations. (a) Without a cavity, on a $300\ \mu\text{m}$ -thick substrate, the emission energy scales linearly with magnetic field. (b) With a $50\ \mu\text{m}$ -thick substrate and resonant cavity, three cavity modes appear around the energies 4, 7, and 10 meV, showing clear coupling to the cyclotron resonance. (c) With a $28\ \mu\text{m}$ -thick cavity, only two modes at 4 and 10 meV are observed, exhibiting stronger anticrossings. (d) The emission peak energies from panel (c), plotted versus magnetic field, align with the reflectivity features labeled UP1 and UP2.

system is in the Shubnikov-de Haas or incipient Landau quantization regime, where Landau levels are present but partially overlap (see SM). Although the cyclotron resonance energy evolves linearly with the magnetic field, the slope of the cyclotron resonance changes with the concentration of electrons. The cyclotron mass extracted from a linear fit is 0.024 times the bare electron mass, which is consistent with the carrier density. In the presence of the cavity, the cyclotron dispersion versus magnetic field B is dramatically modified due to the interaction with two cavity modes with respective photon energies $\hbar\omega_1 \simeq 3\ \text{meV}$ and $\hbar\omega_2 \simeq 10\ \text{meV}$. These interactions result in pronounced energy anticrossings, giving rise to two distinct pairs of Landau upper and lower polariton branches: (UP1, LP1) around $B = 0.7\ \text{T}$ and (UP2, LP2) around 2 T. Fitting these results using the Hopfield polariton model yields excellent agreement, with coupling strengths of $\hbar\Omega_1 = 0.65\ \text{meV}$ and $\hbar\Omega_2 = 0.6\ \text{meV}$.

Electroluminescence – We have investigated cyclotron emission from Dirac electrons in HgTe quantum wells under quantizing magnetic fields by applying short electric pulses that populate high-energy Landau levels with non-equilibrium carriers. Without a cavity, the electroluminescence displays a Gaussian peak that shifts linearly with magnetic field, matching the cyclotron resonance slope from magneto-reflectivity (Figs. 2a and 1a). In contrast, in the presence of a cavity, the emission spectra are markedly modified (Figs. 2b–d). As shown in Fig. 2, the emission is suppressed below the first cavity mode and no longer follows a linear magnetic field dependence. At low fields, the spectrum exhibits discrete peaks corresponding to cavity modes, with fixed positions. This behavior is consistently observed across different samples and cavity thicknesses (see SM). The $50\ \mu\text{m}$ cavity exhibits three

modes around 4, 7, and 10 meV (Fig. 2b), while the $28\ \mu\text{m}$ cavity shows only two modes at 4 and 10 meV (Fig. 2c), where light-matter coupling is stronger. At higher fields, the peaks shift and undergo anticrossings, indicative of polariton formation. In Fig. 2d, the emission peak energies from the $28\ \mu\text{m}$ cavity are plotted as a function of magnetic field. Two distinct inflections correspond to anticrossings at 4 and 10 meV, matching the UP1 and UP2 branches from reflectivity. These results are well reproduced by the Hopfield polariton model, using the same parameters as in magneto-reflectivity. Notably, we can also control the polaritonic anticrossings by applying an electrostatic back gate that tunes the doping density (see SM for more details).

We note that the electroluminescence linewidth exceeds that of absorption. This is expected, as our measurements integrate over all emission angles. Additional broadening may also arise from hot carrier distributions [11], electron-phonon scattering [41], and Stark broadening by ionized impurities [42, 43]. Nevertheless, the emission peak positions closely follow the upper polariton dispersion (Fig. S.7), confirming their origin from Dirac-Landau polaritons. Interestingly, only the upper polariton branch is observed in emission. Thermal black-body radiation can be excluded, as it would favor lower-energy modes. This non-equilibrium behavior may result from a bottleneck effect [44–46] that inhibits polariton relaxation toward lower-energy states. Unlike exciton-polaritons [21], where luminescence is dominated by the lower branch and the bottleneck affects higher-energy states, here the emission favors the upper polariton branches. This may stem from the reduced Landau level energy spacing at high energies, which enhances losses for lower polariton states. Crossed electric and

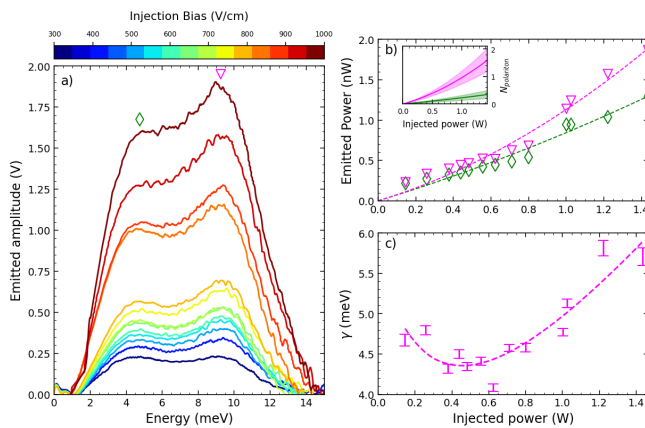


FIG. 3. (a) Electroluminescence spectra measured at $B = 0.9$ T on sample B for different peak-to-peak injection biases ranging from 60 to 200 V. (b) Evolution of the two emission peaks, corresponding to the UP1 and UP2 polariton modes, as a function of the injected electrical power. Marker styles and colors correspond to the peaks shown in (a). Dashed lines represent fits used to extract the polariton population evolution, shown in the inset. (c) Full-width at half maximum (γ) of the UP2 peak (magenta markers) as a function of the injected electrical power P . The dashed line is a fit using the formula given in Eq. 1, which accounts for Schawlow–Townes polariton narrowing and power-induced broadening to lowest order in P .

magnetic fields can further reduce the level spacing at high energy [47], while Coulomb interactions may enable resonant scattering from polaritons to electron-hole excitations. A deeper understanding of these relaxation mechanisms calls for further experimental and theoretical investigation, both in this system and in other Dirac materials.

Polariton stimulation is expected to play a key role when the average number of polaritons per mode is comparable or larger than one. To evaluate the number of polaritons per mode under our experimental conditions, it is first necessary to determine the relevant number of modes. This is achieved by calculating the product of the density of states and the energy corresponding to the emission linewidth (see SM for details). For our setup, the number of modes is approximately 1500. A lower and upper bound for the polariton population in the mode with the highest emission can then be established. The lower bound assumes a uniform distribution of excitations among all the relevant modes. Using this assumption and the emitted power (estimated at 10 nW, see SM), the total number of polaritons is approximately 30. Consequently, the the lowest bound on the number of polaritons per mode at an electric field of 300 V/cm is on the order of 2×10^{-2} . Conversely, the upper bound for the polariton occupation number assumes that all polaritons are concentrated in a single mode. Under this assumption, the number of polaritons per mode ranges from 0.3

to 1.3 at 1 kV/cm, depending on the cavity mode (see insert of Fig. 3b and SM for more details). This upper bound suggests that the system is close to the lasing threshold at 1 kV/cm. However, as we demonstrate below, the polariton occupancy remains in an intermediate regime between the lower and upper bounds.

To investigate this further, we analyzed the influence of the injected electrical power, on the cyclotron emission power (see Fig. 3a). The emitted optical power exhibits a superlinear increase with the injected electrical power across the applied electric field range of 300 to 1000 V/cm (see Fig. 3b), suggesting that while lasing has not yet been achieved under these conditions, the system is approaching the threshold. Another approach to estimating the polariton population is to study the evolution of the emission peak spectral linewidth (full width at half maximum) as the electrical injection bias increases. Fig. 3c shows that the UP2 emission peak spectrally narrows while increasing the electrical power P and reaches a minimum around 0.5 W. Increasing further P the linewidth increases and for power exceeding 0.8 W, there is net broadening with respect to the low-power regime. This could be attributed to non-linear polariton losses caused by scattering processes [48], where a polariton is converted into an excitation of carriers in higher-energy Landau levels, as discussed earlier in the text. We can model in a general way the power-dependent emission linewidth with the formula

$$\gamma(P) = \frac{\gamma(0)}{1 + N_{pol}(P)} + \gamma_{NL}(P), \quad (1)$$

where $N_{pol}(P)$ is the polariton occupation number and $\gamma_{NL}(P)$ is a power-induced additional broadening. This formula includes both Schawlow–Townes narrowing produced by stimulated scattering due to the polariton final-state population and nonlinear losses. At the lowest order in the power, $N_{pol}(P) \simeq \mathcal{N}P$ and $\gamma_{NL}(P) \simeq \eta P$, since both quantities vanish for $P \rightarrow 0$. With this formula we achieve an excellent fit of the experimental linewidth versus power, as shown in Fig. 3c with the fitting parameters $\gamma(0) = 5.65$ meV, $\mathcal{N} = 2.0$ W $^{-1}$ and $\eta = 3.1$ meV/W. For a power $P = 0.5$ W, the estimated polariton occupation number is 1, which is consistent with the previous discussed bounds.

Lasing with Dirac-Landau polaritons offers significant advantages than the ordinary cyclotron excitations. Indeed, the polariton lasing threshold is critically influenced by the loss rate of the polariton modes, which can be optimized by improving both the cavity quality factor and the cyclotron loss rate. Currently, the quality factor of the resonant cavity in our samples is only about $Q \approx 4$ (from the reflectivity spectra). Optimized structures incorporating THz distributed Bragg mirrors around the quantum well, configured as a Tamm cavity [49], could significantly improve performance. Notably, recent THz Tamm cavities have demonstrated quality

factors of $Q = 37$ at 1.5 THz [50], while Landau polariton structures with distributed Bragg reflectors have achieved values exceeding 500 [29]. The enhancements should promisingly lower the stimulation threshold to allow lasing well before the onset of nonlinear losses. The use of Landau polaritons unlocks exciting opportunities for exploring stimulated cyclotron emission in solids. Beyond HgTe quantum wells, this approach enables the consideration of materials previously deemed unsuitable for stimulated emission via the streaming effect [51] due to the requirement for prohibitively high electric fields. By leveraging strong light-matter coupling, these materials can become viable candidates for stimulated emission. More broadly, a wide range of Dirac materials with non-equidistant Landau levels can now be realistically explored for such applications, further expanding the landscape of cyclotron-based light sources and lasers. Notably, spontaneous cyclotron resonance emission in the mid-infrared range was recently demonstrated in electrically biased monolayer graphene [52], underscoring the potential of these mechanisms for future THz and infrared light sources.

Conclusions — We have demonstrated THz electroluminescence from Dirac-Landau polaritons in a regime of strong light-matter coupling between Landau-quantized Dirac fermions and cavity photons. This establishes a platform for exploring cavity quantum electrodynamics in the THz range with relativistic electronic states. The emission occurs under strongly non-equilibrium and nonlinear conditions, with spectral and intensity features consistent with stimulated polariton scattering, indicating proximity to the threshold for polariton lasing. While lasing is not yet achieved, the results demonstrate its feasibility and highlight a clear path toward THz polariton lasers based on Dirac materials, enabled by enhanced cavity quality factors. The distinctive Landau level structure of Dirac systems modifies polariton relaxation and scattering channels compared to conventional semiconductors, offering new directions for investigation. This approach can be extended beyond HgTe quantum wells to a wider class of quantum materials with relativistic carriers.

This work was supported by the Terahertz Occitanie Platform, by the French Agence Nationale pour la Recherche for TEASER project (ANR-24-CE24-4830), by the France 2030 program through and Equipex+ HYBAT project (ANR-21-ESRE-0026), by the CNRS, for the Tremplin 2024 STEP project. We would like to acknowledge E. Chauveau and A. Meguekam for their assistance with substrate thinning. We also thank J. Mangeney, T. Guillet and J. Faist for the valuable discussions. Finally, we wish to extend our gratitude to B. Mongellaz, P. Lefebvre, and I. Philip for their invaluable support in managing the helium recovery service, despite the numerous challenges encountered.

-
- [1] T. Wehling, A. Black-Schaffer, and A. Balatsky, Dirac materials, *Advances in Physics* **63**, 1–76 (2014).
 - [2] A. Tager and A. Gladun, Use of cyclotron resonance in semiconductors for the amplification and generation of microwaves., *Sov. Phys. JETP* **8**, 560 (1959).
 - [3] N. Basov, B. Vul, and Y. Popov, Quantum-mechanical semiconductor generators and amplifiers of electromagnetic oscillations, *Sov. Phys. JETP* **10**, 416 (1960).
 - [4] Y. Kagan, Cyclotron resonance in germanium and silicon and the effect of negative effective masses., *JETP* **11**, 1333 (1960).
 - [5] E. Gornik, G. Strasser, and K. Unterrainer, Landau level laser, *Nature Photonics* **15**, 875–883 (2021).
 - [6] D. B. But, M. Mittendorff, C. Consejo, F. Tepe, N. N. Mikhailov, S. A. Dvoretiskii, C. Faugeras, S. Winnerl, M. Helm, W. Knap, M. Potemski, and M. Orlita, Suppressed Auger scattering and tunable light emission of Landau-quantized massless Kane electrons, *Nature Photonics* **13**, 783–787 (2019).
 - [7] Y. L. Ivanov and Y. V. Vasiljev, Stimulated Landau level emission in p-Ge., *Sov. Tech. Lett.* **9**, 264 (1983).
 - [8] Y. Yu. V. Vasiljev, Yu. L. Ivanov, Light amplification during Landau-level inversion of light germanium holes., *Sov. Tech. Phys. Lett.* **10**, 398–401 (1984).
 - [9] A. A. Andronov, A. M. Belyantsev, V. I. Gavrilenko, E. P. Dodin, E. F. Krasil'nik, V. V. Nikonorov, S. A. Pavlov, and M. M. Shvarts, Germanium hot-hole cyclotron-resonance maser with negative effective hole masses, *JETP* **63**, 211 (1986).
 - [10] S. Komiyama, N. Iizuka, and Y. Akasaka, Evidence for induced far-infrared emission from p-Ge in crossed electric and magnetic fields, *Appl. Phys. Lett.* **47**, 958 (1985).
 - [11] E. Gornik, Landau emission in semiconductors, W. Zawadzki (eds) *Narrow Gap Semiconductors Physics and Applications. Lecture Notes in Physics* **133** (1980).
 - [12] B. A. Bernevig, T. L. Hughes, and S.-C. Zhang, Quantum spin Hall effect and topological phase transition in HgTe quantum wells, *Science* **314**, 1757–1761 (2006).
 - [13] B. Büttner, C. X. Liu, G. Tkachov, E. G. Novik, C. Brüne, H. Buhmann, E. M. Hankiewicz, P. Recher, B. Trauzettel, S. C. Zhang, and L. W. Molenkamp, Single valley Dirac fermions in zero-gap HgTe quantum wells, *Nature Physics* **7**, 418–422 (2011).
 - [14] S. Gebert, C. Consejo, S. S. Krishtopenko, S. Ruffenach, M. Szola, J. Torres, C. Bray, B. Jouault, M. Orlita, X. Baudry, P. Ballet, S. V. Morozov, V. I. Gavrilenko, N. N. Mikhailov, S. A. Dvoretiskii, and F. Tepe, Terahertz cyclotron emission from two-dimensional Dirac fermions, *Nature Photonics* **17**, 244–249 (2023).
 - [15] B. Benhamou-Bui, C. Consejo, S. S. Krishtopenko, M. Szola, K. Maussang, S. Ruffenach, E. Chauveau, S. Benlemqwanssa, C. Bray, X. Baudry, P. Ballet, S. V. Morozov, V. I. Gavrilenko, N. N. Mikhailov, S. A. Dvoretiskii, B. Jouault, J. Torres, and F. Tepe, Gate tunable terahertz cyclotron emission from two-dimensional Dirac fermions, *APL Photonics* **8**, 10.1063/5.0168578 (2023).
 - [16] M. König, S. Wiedmann, C. Brune, A. Roth, H. Buhmann, L. W. Molenkamp, X.-L. Qi, and S.-C. Zhang, Quantum spin Hall insulator state in HgTe quantum wells, *Science* **318**, 766–770 (2007).

- [17] I. Carusotto and C. Ciuti, Quantum fluids of light, *Rev. Mod. Phys.* **85**, 299 (2013).
- [18] A. Imamoglu, R. J. Ram, S. Pau, and Y. Yamamoto, Nonequilibrium condensates and lasers without inversion: Exciton-polariton lasers, *Phys. Rev. A* **53**, 4250 (1996).
- [19] H. Deng, G. Weihs, D. Snoke, J. Bloch, and Y. Yamamoto, Polariton lasing vs. photon lasing in a semiconductor microcavity, *Proceedings of the National Academy of Sciences* **100**, 15318 (2003).
- [20] H. Deng, G. Weihs, C. Santori, J. Bloch, and Y. Yamamoto, Condensation of semiconductor microcavity exciton polaritons, *Science* **298**, 199 (2002).
- [21] J. Kasprzak, M. Richard, S. Kundermann, A. Baas, P. Jeambrun, J. M. J. Keeling, F. M. Marchetti, M. H. Szymanska, R. Andre, J. L. Staehli, V. Savona, P. B. Littlewood, B. Deveaud, and L. S. Dang, Bose-Einstein condensation of exciton polaritons, *Nature* **443**, 409–414 (2006).
- [22] R. Balili, V. Hartwell, D. Snoke, L. Pfeiffer, and K. West, Bose-Einstein condensation of microcavity polaritons in a trap, *Science* **316**, 1007 (2007).
- [23] C. Schneider, A. Rahimi-Iman, N. Y. Kim, J. Fischer, I. G. Savenko, M. Amthor, M. Lermer, A. Wolf, L. Worschech, V. D. Kulakovskii, I. A. Shelykh, M. Kamp, S. Reitzenstein, A. Forchel, Y. Yamamoto, and S. Höfling, An electrically pumped polariton laser, *Nature* **497**, 348–352 (2013).
- [24] T.-C. Lu, Y.-Y. Lai, Y.-P. Lan, S.-W. Huang, J.-R. Chen, Y.-C. Wu, W.-F. Hsieh, and H. Deng, Room temperature polariton lasing vs. photon lasing in a ZnO-based hybrid microcavity, *Opt. Express* **20**, 5530 (2012).
- [25] P. Bhattacharya, T. Frost, S. Deshpande, M. Z. Baten, A. Hazari, and A. Das, Room temperature electrically injected polariton laser, *Phys. Rev. Lett.* **112**, 236802 (2014).
- [26] W.-H. Xu, Y.-H. Chou, Z.-Y. Yang, Y.-Y. Liu, M.-W. Yu, C.-H. Huang, C.-T. Chang, C.-Y. Huang, T.-C. Lu, T.-R. Lin, and K.-P. Chen, Tamm plasmon-polariton ultraviolet lasers, *Advanced Photonics Research* **3**, 2100120 (2022).
- [27] D. Hagenmüller, S. De Liberato, and C. Ciuti, Ultrastrong coupling between a cavity resonator and the cyclotron transition of a two-dimensional electron gas in the case of an integer filling factor, *Phys. Rev. B* **81**, 235303 (2010).
- [28] G. Scalari, C. Maissen, D. Turcinkova, D. Hagenmüller, S. D. Liberato, C. Ciuti, C. Reichl, D. Schuh, W. Wegscheider, M. Beck, and J. Faist, Ultrastrong coupling of the cyclotron transition of a 2D electron gas to a THz metamaterial, *Science* **335**, 1323 (2012).
- [29] Q. Zhang, M. Lou, X. Li, J. L. Reno, W. Pan, J. D. Watson, M. J. Manfra, and J. Kono, Collective non-perturbative coupling of 2D electrons with high-quality-factor terahertz cavity photons, *Nature Physics* **12**, 1005–1011 (2016).
- [30] V. M. Muravev, I. V. Andreev, I. V. Kukushkin, S. Schmult, and W. Dietsche, Observation of hybrid plasmon-photon modes in microwave transmission of coplanar microresonators, *Physical Review B* **83**, 10.1103/physrevb.83.075309 (2011).
- [31] G. L. Paravicini-Bagliani, F. Appugliese, E. Richter, F. Valmorra, J. Keller, M. Beck, N. Bartolo, C. Rössler, T. Ihn, K. Ensslin, C. Ciuti, G. Scalari, and J. Faist, Magneto-transport controlled by Landau polariton states, *Nature Physics* **15**, 186–190 (2018).
- [32] J. Keller, G. Scalari, F. Appugliese, S. Rajabali, M. Beck, J. Haase, C. A. Lehner, W. Wegscheider, M. Failla, M. Myronov, D. R. Leadley, J. Lloyd-Hughes, P. Nataf, and J. Faist, Landau polaritons in highly nonparabolic two-dimensional gases in the ultrastrong coupling regime, *Phys. Rev. B* **101**, 075301 (2020).
- [33] F. Appugliese, J. Enkner, G. L. Paravicini-Bagliani, M. Beck, C. Reichl, W. Wegscheider, G. Scalari, C. Ciuti, and J. Faist, Breakdown of topological protection by cavity vacuum fields in the integer quantum Hall effect, *Science* **375**, 1030 (2022).
- [34] K. Kuroyama, J. Kwoen, Y. Arakawa, and K. Hirakawa, Electrical detection of ultrastrong coherent interaction between terahertz fields and electrons using quantum point contacts, *Nano Letters* **23**, 11402–11408 (2023).
- [35] K. Kuroyama, J. Kwoen, Y. Arakawa, and K. Hirakawa, Coherent interaction of a few-electron quantum dot with a terahertz optical resonator, *Phys. Rev. Lett.* **132**, 066901 (2024).
- [36] V. M. Muravev, I. V. Andreev, N. D. Semenov, P. A. Gusikhin, and I. V. Kukushkin, Absorption of electromagnetic waves in a screened two-dimensional electron system, *Physical Review B* **110**, 10.1103/physrevb.110.205416 (2024).
- [37] D. Hagenmüller and C. Ciuti, Cavity QED of the graphene cyclotron transition, *Phys. Rev. Lett.* **109**, 267403 (2012).
- [38] L. Chirolli, M. Polini, V. Giovannetti, and A. H. MacDonald, Drude weight, cyclotron resonance, and the Dicke model of graphene cavity QED, *Phys. Rev. Lett.* **109**, 267404 (2012).
- [39] G. M. Andolina, M. Ceccanti, B. Turini, R. Riolo, M. Polini, M. Schiro, and F. H. L. Koppens, Quantum electrodynamics of graphene Landau levels in a deep-subwavelength hyperbolic phonon polariton cavity 10.48550/ARXIV.2501.04133 (2025).
- [40] C. Ciuti, G. Bastard, and I. Carusotto, Quantum vacuum properties of the intersubband cavity polariton field, *Phys. Rev. B* **72**, 115303 (2005).
- [41] C. Chaubet, A. Raymond, and D. Dur, Heating of two-dimensional electrons by a high electric field in a quantizing magnetic field: Consequences in Landau emission and in the quantum Hall effect, *Phys. Rev. B* **52**, 11178 (1995).
- [42] J. C. Hensel and M. Peter, Stark effect for cyclotron resonance in degenerate bands, *Phys. Rev.* **114**, 411 (1959).
- [43] E. Gornik, R. Schawarz, G. Lindemann, and D. Tsui, Emission spectroscopy on two-dimensional systems, *Surface Science* **98**, 493 (1980).
- [44] F. Tassone, C. Piermarocchi, V. Savona, A. Quattropani, and P. Schwendimann, Bottleneck effects in the relaxation and photoluminescence of microcavity polaritons, *Phys. Rev. B* **56**, 7554 (1997).
- [45] F. Tassone and Y. Yamamoto, Exciton-exciton scattering dynamics in a semiconductor microcavity and stimulated scattering into polaritons, *Phys. Rev. B* **59**, 10830 (1999).
- [46] L. S. Dang, D. Heger, R. André, F. Bœuf, and R. Romestain, Stimulation of polariton photoluminescence in semiconductor microcavity, *Phys. Rev. Lett.* **81**, 3920 (1998).
- [47] W. Zawadzki, Semiconductor electrons in electric and magnetic fields, *Surface Science* **37**, 218 (1973).
- [48] D. Porras and C. Tejedor, Linewidth of a polariton laser:

- Theoretical analysis of self-interaction effects, *Phys. Rev. B* **67**, 161310 (2003).
- [49] X. Li, M. Bamba, Q. Zhang, S. Fallahi, G. C. Gardner, W. Gao, M. Lou, K. Yoshioka, M. J. Manfra, and J. Kono, Vacuum Bloch–Siegert shift in Landau polaritons with ultra-high cooperativity, *Nature Photonics* **12**, 324–329 (2018).
- [50] S. Messelot, S. Coeymans, J. Tignon, S. Dhillon, and J. Mangeney, High Q and sub-wavelength THz electric field confinement in ultrastrongly coupled THz resonators, *Photon. Res.* **11**, 1203 (2023).
- [51] S. Komiyama, Streaming motion and population inversion of hot carriers in crossed electric and magnetic fields, *Advances in Physics* **31**, 255–297 (1982).
- [52] F. Inamura, G. Ueda, S. Kim, M. Patrashin, I. Hosako, S. Komiyama, and K. Ikushima, Landau-level terahertz emission from electrically biased graphene, *APL Photonics* **9**, 10.1063/5.0233487 (2024).
- [53] J. C. Cuevas, Thermal radiation from subwavelength objects and the violation of Planck’s law, *Nature Communications* **10**, 10.1038/s41467-019-11287-6 (2019).
- [54] R. Fenollosa, F. Ramiro-Manzano, M. Garin, and R. Alcubilla, Thermal emission of silicon at near-infrared frequencies mediated by Mie resonances, *ACS Photonics* **6**, 3174 (2019).
- [55] B. Liu, W. Gong, B. Yu, P. Li, and S. Shen, Perfect thermal emission by nanoscale transmission line resonators, *Nano Letters* **17**, 666 (2017), pMID: 28045267.
- [56] Q. Chu, F. Zhang, Y. Zhang, T. Qiao, S. Zhu, and H. Liu, Integrated thermal emission microchip based on meta-cavity array, *Nanophotonics* **11**, 4263 (2022).
- [57] R.-J. Shiue, Y. Gao, C. Tan, C. Peng, J. Zheng, D. K. Efetov, Y. D. Kim, J. Hone, and D. Englund, Thermal radiation control from hot graphene electrons coupled to a photonic crystal nanocavity, *Nature Communications* **10**, 10.1038/s41467-018-08047-3 (2019).

**Supplementary Material for the article:
“Nonlinear Terahertz electroluminescence from Dirac-Landau polaritons“**

B. Benhamou-Bui¹, C. Consejo¹, S.S. Krishtopenko¹, S. Ruffenach¹, C. Bray¹, J. Torres¹, J. Dzian², F. Le Mardelé², A. Pagot³, X. Baudry³, S.V. Morozov^{4,5}, N.N.

Mikhailov^{6,7}, S.A. Dvoretiskii^{7,8}, B. Jouault¹, P. Ballet³, M. Orlita², C. Ciuti⁹, F. Teppe¹

¹ *Laboratoire Charles Coulomb (L2C), UMR 5221 CNRS – Université de Montpellier, F-34095 Montpellier, France*

² *Laboratoire National des Champs Magnétiques Intenses, CNRS – UGA – UPS – INSA – EMFL, Grenoble, France*

³ *CEA, LETI, MINATEC Campus, DOPT, Grenoble, France*

⁴ *Institute for Physics of Microstructures of the Russian Academy of Sciences, Nizhny Novgorod, Russia*

⁵ *Lobachevsky State University of Nizhny Novgorod, Nizhny Novgorod, Russia*

⁶ *A.V. Rzhanov Institute of Semiconductor Physics, Siberian Branch of the Russian Academy of Sciences, Novosibirsk, Russia*

⁷ *Novosibirsk State University, Novosibirsk, Russia*

⁸ *Tomsk State University, Tomsk, Russia and*

⁹ *Université Paris Cité, CNRS, Matériaux et Phénomènes Quantiques, 75013 Paris, France*

(Dated: May 8, 2025)

This Supplementary Material provides additional information on the experimental techniques, sample structure, cavity and polariton modeling, and data analysis methods that support the main findings of the manuscript. It includes: (i) a detailed description of the samples and the measurement protocols for electroluminescence and reflectivity; (ii) modeling and extraction procedures for Landau polariton coupling; (iii) quantitative estimates of the polariton population; and (iv) additional experimental data on the gate-voltage dependence of the emission and the cavity-induced spectral shaping.

METHODS

Samples

Two types of samples were studied, both grown via Molecular Beam Epitaxy (MBE) on GaAs-(013) or CdTe-(100) substrates (see Table I for details). Two distinct buffer layers were employed, as illustrated in Figure S.1. The active layer consists of a HgTe QW with HgCdTe barriers, with only one sample type incorporating a CdTe cap layer. To create an optical cavity, the substrates were thinned below 50 μm using two techniques: (i) micrometric rotary sawing down to 40 μm or (ii) mechanical polishing to 50 μm , followed by inductively coupled plasma etching to further reduce the thickness below 30 μm . The samples were then mounted on a gold sample holder.

Landau emission measurement technique

Higher Landau levels are populated using short electrical pulses with a frequency of 127 Hz, peak-to-peak amplitudes ranging from 40 V to 200 V, and durations between 1 ms and 30 μs . These pulses are applied to the sample via indium balls soldered onto its surface, which diffuse into the structure, forming high-quality ohmic contacts. The experimental setup includes a Landau spectrometer with three superconducting coils housed in a liquid helium cryostat (see [14] for details). The detector is an n -type InSb bolometer, which operates under a strong magnetic field to refine and narrow its detection energy window. The second coil resolves the LL structure of the sample, while the third coil decouples the contributions of the first two fields.

The measurement protocol involves fixing the sample’s magnetic field while sweeping the detector’s magnetic field, enabling energy spectra acquisition at a constant sample field. The detector signal is amplified by a low-noise amplifier and processed via a boxcar averager, ensuring a high signal-to-noise ratio even for low-duty-cycle pulses ranging from 0.4% to 1%. All measurements were performed at 4.2 K.

Cavity characterization

When the substrate is thin, i.e. on the order of $\lambda/2$ for the cyclotron wavelength, the emission spectrum is strongly modified by the presence of cavity electromagnetic modes. The metal contact placed on the back side of the sample and the helium/semiconductor interface on the front side act as mirrors for a vertical resonant

Sample name	Substrate	Thickness	Cavity mode energies	Carriers density [cm^{-2}]
Sample A	GaAs	28 μm	3.1 meV ; 10 meV	7×10^{11}
Sample B	GaAs	30 μm	3.8 meV ; 9.5 meV	$\times 10^{11}$
Sample C	CdTe	40 μm	5 meV ; 9 meV	3×10^{11}

TABLE I. Table summarizing the different samples' characteristics.

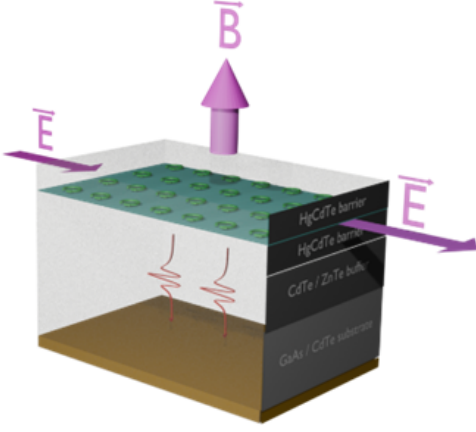


FIG. S.1. **Schematic representation of the sample layer structure.** The core consists of a HgTe quantum well (QW) sandwiched between HgCdTe barriers with a Cd composition of 68%. A CdTe/ZnTe buffer layer is inserted beneath the QW to facilitate strain relaxation before reaching the substrate.

THz cavity. In order to characterize the cavity effect, we performed emission measurements at zero magnetic field. When the LLs are not yet established, the emission spectrum is not related with the CR and is primarily composed of blackbody radiation, most likely originating from the heating of the current injection contacts. When the dimensions of a thermally emitting object are on the order of the thermal radiation wavelength λ_{Th} , its emission can indeed substantially differ from the predictions made by Planck's law [53, 54], creating new possibilities in the realm of thermal radiation. For instance, the presence of some Fabry-Pérot cavity modes can greatly enhance thermal emission, producing a narrow-band emission spectrum consistent with the Purcell effect. Moreover, the spectral emission power can exceed the limits imposed by Planck's law for blackbody radiation [55].

Figure S.2 below shows these emission spectra plotted for the different sample thicknesses. When the substrate is thick, the blackbody emission spectrum is broadband, and its peak is, as expected, red shifted as the injection current decreases. When the substrate is reduced to thicknesses comparable to the wavelength of thermal radiation defined by Wien's displacement law, the broadband blackbody radiation transforms, uncovering peaks at energies aligned with the substrate's optical cavity modes. The interaction between the resonant modes of

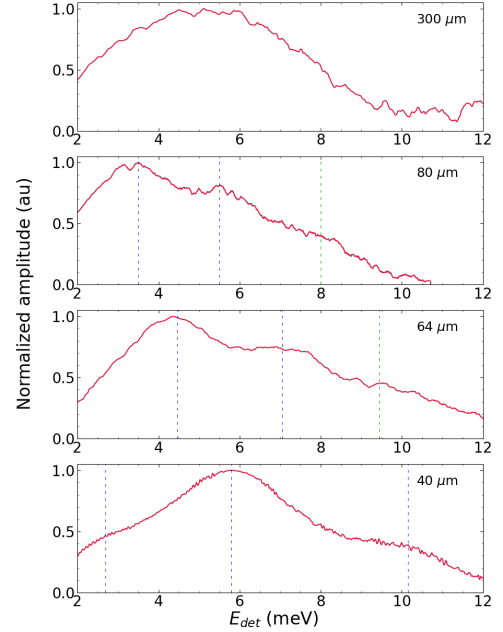


FIG. S.2. **Emission spectra obtained at 4.2 K, at zero magnetic field, on sample A, for different substrate thicknesses.** On the bare sample (300 μm), the spectrum exhibits no structuration. When the substrate thickness is reduced below 100 μm , additional extrema (blue dashed lines) emerge, indicating a cavity effect. Notably, the 8 meV line in the 80 μm sample and the 9.5 meV line in the 64 μm sample (grey dashed lines) are barely visible at $B = 0$ T but become observable through cyclotron resonance at finite magnetic fields.

the cavity induces a narrower thermal emission bandwidth [56, 57]. Indeed, since the sample acts at zero magnetic field as both a thermal heat source and an optical cavity, its thermal radiation is modulated by the cavity modes according to the Purcell effect.

The emission signal is structured into a series of peaks, with their positions varying depending on the substrate thickness. We then compare in Figure S.3 these energy positions with a simulation using the Transfer Matrix Method (TMM) [50]. Taking into account the sample geometry (thinned substrate on a gold sample holder) and the complex refractive index of the material, we were able to accurately reconstruct the energy positions of the modes for the different thicknesses. There is excellent agreement between the experimental data and the simulation, as the theoretical thicknesses used to reproduce

the results closely match those measured experimentally.

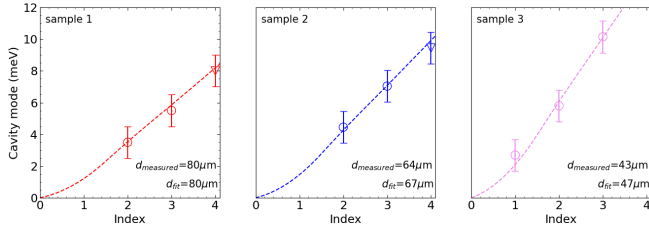


FIG. S.3. **Evolution of cavity mode energies extracted from Fig. SM2 for three different samples with varying substrate thicknesses (empty circles).** Triangular markers correspond to data obtained at high magnetic fields. The energy values were deduced from the $B = 0$ T emission spectra. A Transfer Matrix Method (TMM) prediction (dashed lines) is overlaid, showing excellent agreement with the experimental data.

Another way to characterize the cavity effect induced by the substrate is to perform room temperature THz reflectivity thanks to a commercial Time-Domain-Spectroscopy (TDS) setup. Figure S.4 below shows two spectra obtained on the two thinnest samples. It clearly displays some reflectivity minima, well corresponding to the cavity modes. These minima positions, when extracted, are once again in a very good agreement with the TMM simulations.

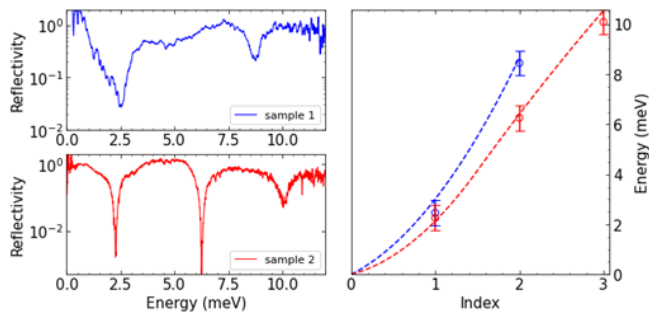


FIG. S.4. **THz reflectivity and transmission analysis.** (Left panel) TDS reflectivity spectra measured for samples A and B. (Right panel) Transmission minima extracted and plotted against an arbitrary index (empty circles). A TMM-based prediction (dashed lines) is overlaid, showing excellent agreement with the experimental data.

Magneto-transport measurements – Shubnikov-de Haas regime

The electron densities of the samples are determined using the standard Shubnikov-de Haas magneto-transport technique. Figure S.5 below presents the typical magneto-resistance behavior of our samples. The observed oscillations enable us to extract the electron density via the well-known formula:

$$n_S = \frac{e}{h \cdot \Delta(1/B)}, \quad (\text{S.1})$$

where $\Delta(1/B)$ is the inverse magnetic field period of the oscillations. For the sample shown below, this yields $n_S = 7.0 \times 10^{11} \text{ cm}^{-2}$.

Additionally, cyclotron resonance measurements allow us to determine the cyclotron mass of the sample (see main text). By combining these results, we can verify the predicted evolution of the cyclotron mass as a function of electron density, as derived from the low-energy model[14]. The inset demonstrates excellent agreement between the experimental data and the theoretical model.

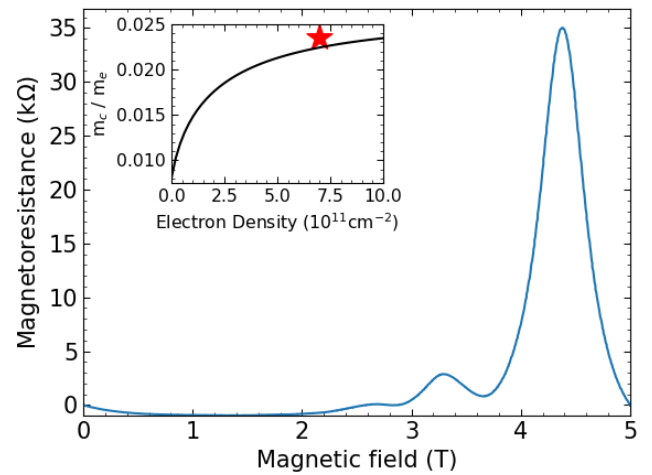


FIG. S.5. **Longitudinal magneto-resistance and cyclotron mass evolution.** Shubnikov-de Haas oscillations measured in the longitudinal magneto-resistance of sample A. (Inset) Theoretical dependence of the cyclotron mass on electron density, based on a low-energy model [14]. The red star represents the experimental value extracted from reflectivity and magneto-transport measurements, showing consistency with theoretical predictions.

Regarding the magneto-reflectivity and cyclotron emission results, it is important to note that the system operates within the Shubnikov-de Haas regime. This implies that the Landau levels (LLs) are already present but still exhibit partial overlap. These conditions, which lie between the classical and quantum regimes, are often referred to as the incipient Landau quantization regime.

Similar to the classical case, the cyclotron resonance (CR) energy evolves linearly with the applied magnetic field. This occurs because, as the magnetic field increases, the Fermi level oscillates between adjacent LLs. Consequently, even though the LLs in the system are relativistic and follow a \sqrt{B} dependence, the energy of optical transitions between these levels remains linear in the magnetic field. This can be understood by considering the energy difference between two adjacent LLs, $n+1$

and n :

$$\hbar\omega_c = \sqrt{2v_F^2 eB \hbar} (\sqrt{n+1} - \sqrt{n}) \text{ with } E_F = \sqrt{2v_F^2 eB \hbar} \sqrt{n}. \quad (\text{S.2})$$

Considering that for $n \gg 1$

$$\sqrt{n+1} - \sqrt{n} \simeq \frac{1}{2\sqrt{n}}, \quad (\text{S.3})$$

we finally have

$$\begin{aligned} \hbar\omega_c &= \sqrt{2v_F^2 eB \hbar} (\sqrt{n+1} - \sqrt{n}) \\ &\simeq \sqrt{2v_F^2 eB \hbar} \frac{1}{2\sqrt{n}} \\ &= \frac{2v_F^2 eB \hbar}{2E_F} = \frac{eB \hbar}{m_c}, \end{aligned} \quad (\text{S.4})$$

where we defined $m_c = \frac{E_F}{v_F^2}$.

Landau polariton: Fitting procedure

To extract the coupling strength from the reflectivity measurements, we followed the same procedure as in [28]. It is based on the following total Hopfield Hamiltonian [27]:

$$H = H_{cavity} + H_{Landau} + H_{int} + H_{dia}, \quad (\text{S.5})$$

where H_{cavity} is the bare Hamiltonian of the cavity, H_{Landau} describes the collective cyclotron excitation of the electrons occupying the Landau levels, H_{int} is the paramagnetic light-matter interaction, while H_{dia} is the diamagnetic contribution. The polariton excitations can be obtained by diagonalizing the following Hopfield-Bogoliubov matrix:

$$M_j(B, \chi_j) = \hbar \begin{pmatrix} \omega_c & \chi_j \sqrt{\omega_c} & 0 & \chi_j \sqrt{\omega_c} \\ \chi_j \sqrt{\omega_c} & \omega_j + 2\chi_j^2 & \chi_j \sqrt{\omega_c} & 2\chi_j^2 \\ 0 & -\chi_j \sqrt{\omega_c} & -\omega_c & -\chi_j \sqrt{\omega_c} \\ -\chi_j \sqrt{\omega_c} & -2\chi_j^2 & -\chi_j \sqrt{\omega_c} & -\omega_j - 2\chi_j^2 \end{pmatrix}, \quad (\text{S.6})$$

where

$$\chi_j = \frac{\Omega_j}{\sqrt{\omega_c}} \quad (\text{S.7})$$

is a fitting parameter, independent of the magnetic field, Ω_j being the collective polariton coupling (Rabi) frequency for the electromagnetic mode j . By diagonalizing this Hamiltonian, we can access the theoretical polaritonic branches, labelled $\omega_j^{UP}(B, \chi)$ (resp. $\omega_j^{LP}(B, \chi)$) for the upper branch (resp. lower branch). Therefore, we can extract the coupling strength by minimizing the quantity

$$RMSD_j(\chi) = \sqrt{\frac{\sum_{\chi}^{N_{exp}} \left[(\omega_{j,\eta}^{UP} - \omega_j^{UP}(B_\eta, \chi))^2 + (\omega_{j,\eta}^{LP} - \omega_j^{LP}(B_\eta, \chi))^2 \right]}{2N_{exp}}}, \quad (\text{S.8})$$

where N_{exp} is the number of experimentally measured points. One example of minimization is shown in Fig. S.6.

Estimation of the number of polaritons per mode

Lower bound estimate

Let us consider the cavity energy dispersion

$$E_{cav}(k) = \frac{\hbar c}{n} \sqrt{k_z^2 + k^2}, \quad (\text{S.9})$$

where c is the speed of light, n the refractive index of the substrate, z is the direction perpendicular to the 2D

material. For small in-plane wave vectors, the cavity dispersion can be approximated as parabolic, namely:

$$E_{cav}(k) = \frac{\hbar c}{n} k_z \sqrt{1 + \frac{k^2}{k_z^2}} \simeq E_{cav}(0) \left(1 + \frac{1}{2} \frac{k^2}{k_z^2} \right). \quad (\text{S.10})$$

The density of photonic states is

$$\begin{aligned} \mathcal{D}(E) &\simeq \frac{A}{(2\pi)^2} \int d^2k \delta(E - E_{cav}(k)) \\ &= \frac{A}{2\pi} \int k dk \delta(E - E_{cav}(k)), \end{aligned} \quad (\text{S.11})$$

where A is the area of sample where there is emission. Since $dE_{cav} = E_{cav}(0) \frac{k dk}{k_z^2}$, then $k dk = \frac{k_z^2}{E_{cav}(0)} dE_{cav}$ and

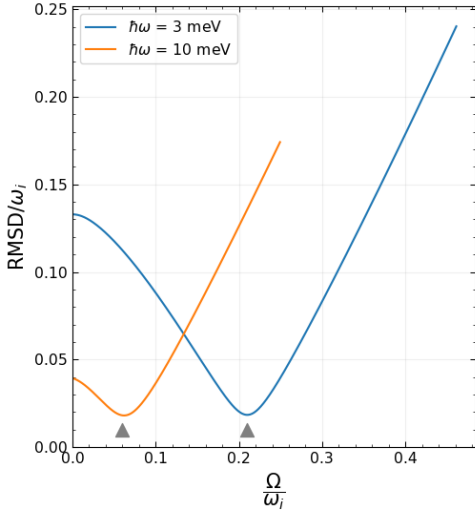


FIG. S.6. **Normalized root-mean-square deviation analysis for sample A.** Evolution of the normalized root-mean-square deviation for the two electromagnetic modes. The minima correspond to normalized coupling strengths of 21% and 4% for the lower and higher modes, respectively, indicating distinct interaction regimes.

therefore

$$\mathcal{D}(E) \simeq \frac{A}{2\pi} \frac{k_z^2}{E_{cav}(0)}. \quad (\text{S.12})$$

The polariton density of states is comparable to the photonic density of states, which will be used for our estimate of the number of polariton modes involved in the emission process:

$$\mathcal{N}_{mode} \simeq \mathcal{D}(E) \Delta E_{emission} = \frac{A}{2\pi} k_z^2 \frac{\Delta E_{emission}}{E_{cav}(0)}, \quad (\text{S.13})$$

where ΔE_{em} is the emission linewidth. Given the experimental nominal parameters, we can take $A \simeq 1 \text{ mm}^2$, $k_z = \frac{\pi}{L_{cav}} = \frac{\pi}{30 \mu\text{m}} = 10^5 \text{ m}^{-1}$ and $\Delta E_{emission} = 3 \text{ meV}$ we have $E_{cav}(0) \simeq 3 \text{ meV}$ we get $\mathcal{N}_{mode} \simeq 1500$. Finally, we can estimate the number of polariton via the emitted power:

$$\mathcal{P}^{emission} \simeq N_{pol} \gamma_{rad}^{avg} \hbar \omega_{pola}^{avg}, \quad (\text{S.14})$$

where N_{pol} is the number of polaritons in the steady state, γ_{rad}^{avg} the average radiative rate and $\hbar \omega_{pola}^{avg}$ the average photon emission energy. By injecting the experimental values $\mathcal{P}^{emission} \simeq 10 \text{ nW}$, $\hbar \omega_{pola}^{avg} \simeq 3 \text{ meV}$ and $\gamma_{rad}^{avg} \simeq \frac{\Delta E_{emission}}{h} = \frac{3 \text{ meV}}{h} \simeq 0.7 \text{ ps}^{-1}$ we get: $N_{pol} \simeq 30$. Finally, we get the lower bound:

$$\frac{N_{pol}}{\mathcal{N}_{mode}} > 2 \cdot 10^{-2}. \quad (\text{S.15})$$

Upper bound estimate

The upper bound for the polariton occupation number is obtained by assuming that all the polaritons are occupying the same polariton mode. This is certainly not the case, but together with the lower bound calculated above will allow us to have a decent estimate of the polariton occupation numbers. Assuming that only one mode participates to the emission, we can estimate the polariton population from the non-linear dependence of the emission amplitude with respect to the injected electrical power. This can be calculated via the simple rate equation:

$$\frac{dN_{pol}}{dt} \simeq -\gamma N_{pol} + \eta V_{pp}(1 + N_{pol}), \quad (\text{S.16})$$

where γ is the polariton loss rate and η is unknown. The steady-state solution reads:

$$N_{pol} = \frac{\eta V_{pp}}{\gamma - \eta V_{pp}}. \quad (\text{S.17})$$

From this equation we can see that for $P_{elec} \rightarrow P_{elec}^{(thresholds)} = \frac{\gamma}{\eta}$ then $N_{pol} \rightarrow +\infty$. Below threshold, we can Taylor-expand the previous solution as follows:

$$\begin{aligned} N_{pol} &= \frac{\eta P_{elec}}{\gamma} \frac{1}{1 - \frac{\eta P_{elec}}{\gamma}} \simeq \frac{\eta P_{elec}}{\gamma} \left(1 + \frac{\eta P_{elec}}{\gamma}\right) \\ &\simeq \frac{\eta P_{elec}}{\gamma} + \left(\frac{\eta P_{elec}}{\gamma}\right)^2. \end{aligned} \quad (\text{S.18})$$

Therefore, we now have the dependence of the emission power on the electrical power, namely

$$\begin{aligned} P^{emission} &\simeq N_{pol} \gamma_{rad}^{avg} \hbar \omega_{pola}^{avg} \\ &\simeq \gamma_{rad}^{avg} \hbar \omega_{pola}^{avg} \left[\frac{\eta P_{elec}}{\gamma} + \left(\frac{\eta P_{elec}}{\gamma}\right)^2 \right] = a_1 P_{elec} + a_2 P_{elec}^2, \end{aligned} \quad (\text{S.19})$$

where $a_2/a_1 = \gamma/\eta$. We can therefore have access to the polariton population by fitting the curve corresponding to the measured emitted power versus the electrical injected power, as shown in the figure 3 in the main text. For the considered sample, the polariton population would reach more than one for an electrical injected power of 1.5 W (obtained for an electric field of 1 kV/cm).

From the two scenarios developed above, we can conclude that the polariton occupation from the most populated mode in our system is bound as follows:

$$2 \cdot 10^{-2} \leq N_{pol} \leq \simeq 1. \quad (\text{S.20})$$

Emission / transmission comparison

The figure S.7 shows an emission spectrum on top of reflectivity one, for the same sample and magnetic field

value. It highlights the fact that the emission maximum is aligned with the upper branch of the Landau polariton and that the lower branch remains invisible in emission.

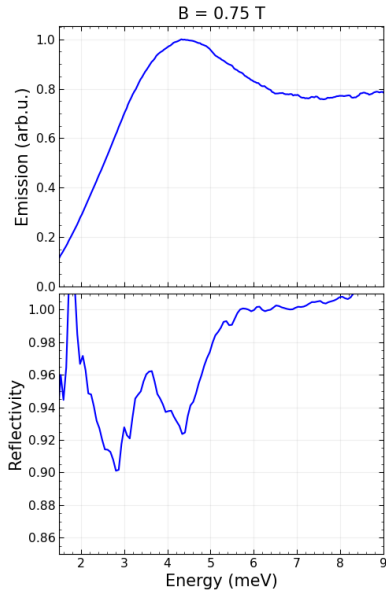


FIG. S.7. **Comparison of emission and transmission spectra at 0.75 T for sample A.** (Top) Emission spectrum measured at a magnetic field of 0.75 T. (Bottom) Corresponding transmission spectrum obtained under the same conditions. The data clearly reveal that only the upper branch of the Landau polariton exhibits significant emission, highlighting the asymmetric population of polariton branches.

Gate voltage effect

Dirac-Landau polaritons exhibit distinctive features compared to the standard Landau polaritons. Because the effective mass of Dirac electrons depends on the electron density, the cyclotron mass and, consequently, the CR slope are continuously tunable via the back-gate voltage. Therefore, the critical magnetic field at which the anticrossing occurs can also be tuned by adjusting the gate voltage (see S.8). Even more interestingly, since the coupling strength term depends on the cyclotron mass, it can be tuned as well with the gate voltage, as illustrated in the insert of S.8. According to the Hopfield polariton model, where the cyclotron mass is derived from the Bernevig-Hughes-Zhang (BHZ) model, the coupling strength can reach 30% in this non-optimized system, for a realistic carrier density of $1 \times 10^{12} \text{ cm}^{-2}$.

The figure S.9 displays two raw emission spectra obtained for two extremes gate bias value of +100 and -100 V and for the same magnetic field value. It highlights the specificity of Dirac materials which is a density-dependent mass inducing a shift of the CR energy and therefore a shift of the Landau polariton anti-crossing.

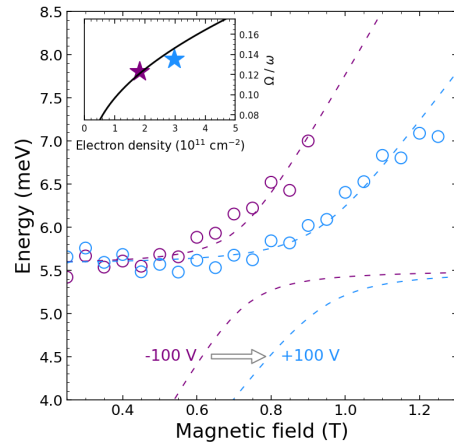


FIG. S.8. **Influence of the gate voltage on coupling strength and critical magnetic field.** Due to the relativistic nature of charge carriers, their concentration in the QW determines the cyclotron mass and thus the slope of the Landau emission. By tuning the carrier density from $n_s = 1.83 \times 10^{11} \text{ cm}^{-2}$ to $2.98 \times 10^{11} \text{ cm}^{-2}$, the cyclotron mass increases, shifting the critical magnetic field for the anticrossing from approximately 0.7 T to 0.9 T. (Main) Extracted emission maxima from spectra measured at different magnetic field values for sample C, with a gate bias of -100 V (purple empty circles) and $+100 \text{ V}$ (blue empty circles). The dashed lines represent fits based on the model developed in Ref.28. (Inset) Evolution of the reduced coupling strength as a function of electron density (black line), based on the model in Ref.28 and the low-energy model describing the cyclotron mass dependence on density [15]. The violet (resp. blue) star represents the extracted reduced coupling strength from the emission curve for a gate bias of -100 V (resp. $+100 \text{ V}$). The model has been rescaled to match the experimental values.

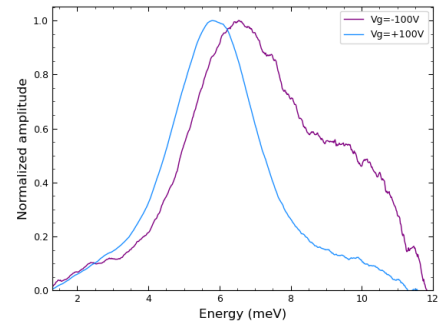


FIG. S.9. **Gate voltage influence on Landau polariton emission.** Emission spectra recorded at a magnetic field of 0.8 T for sample B, with a gate bias of -100 V (purple curve) and $+100 \text{ V}$ (blue curve). As the bias shifts from -100 V to $+100 \text{ V}$, the upper branch of the Landau polariton undergoes a redshift of nearly 1 meV, attributed to the increase in cyclotron mass with higher electron density.

Amplitude and FWHM extraction

To extract the amplitude and the FWHM of the different emission peaks, we used a double-Gaussian fit for every injection bias value. The figure S.10 shows the 13 fits obtained on the experimental spectra.

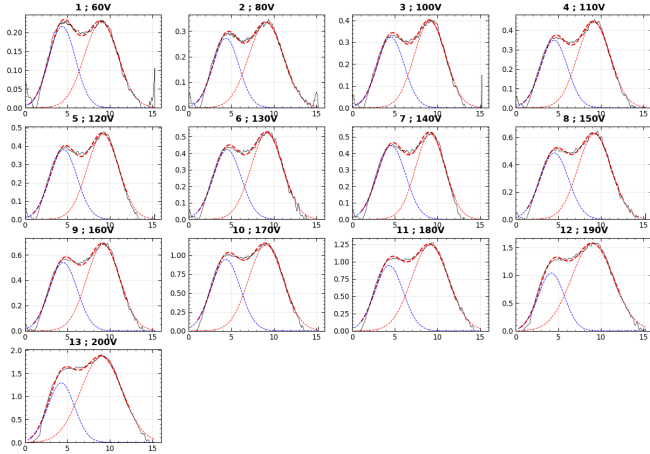


FIG. S.10. **Bias-dependent emission spectra at 0.9 T for sample A.** Emission spectra recorded for different injected bias values. The total double-Gaussian fit is overlaid (red dashed line), along with the individual Gaussian components corresponding to the UP1 (blue dotted line) and UP2 (red dotted line) polariton branches.